https://doi.org/10.1016/j.bios.2021.113214

Ultra-sensitive photoelectrochemical aptamer biosensor for detecting E. coli O157:H7 based on nonmetallic plasmonic two-dimensional hydrated defective tungsten oxide nanosheets coupling with nitrogen-doped graphene quantum dots ($dWO_3 \bullet H_2O$@N-GQDs)

Ding Jiang,[a,b] Cuiqi Yang,[a] Yadi Fan,[a] Hang-Mei Polly Leung,[c] Inthavong Kiao,[d] Yu Zhang,[d] Zhiyang Li,[e] Mo Yang [a,*]

a Department of Biomedical Engineering, The Hong Kong Polytechnic University, Hong Kong, P. R. China

b Jiangsu Key Laboratory of Advanced Catalytic Materials and Technology, School of Petrochemical Engineering, Changzhou University, Changzhou 213164, China

[c] Department of Health Technology and Informatics, The Hong Kong Polytechnic University, Hong Kong, P. R. China

[d]Department of Mechanical and Automotive Engineering, Royal Melbourne Institute of Technology

[e] Department of Clinical Laboratory, the Affiliated Drum Tower Hospital of Nanjing University Medical School, Nanjing 210008, China

*Corresponding author: Prof. Mo Yang, Department of Biomedical Engineering, the Hong Kong Polytechnic University, Hung Hom, Kowloon, Hong Kong, P.R. China. E-mail: Mo.Yang@polyu.edu.hk; Phone: 852-2766-4946; Fax: 852-2334-2429

Abstract

Light absorption and interfacial engineering of photoactive materials play vital roles in photoexcited electron generation and electron transport, and ultimately boost the performance of photoelectrochemical (PEC) biosensing. In this work, a novel high-performance photoelectrochemical (PEC) biosensing platform was fabricated based on nonmetallic plasmonic tungsten oxide hydrate nanosheets (WO_3•H_2O) coupling with nitrogen doped graphene quantum dots (N-GQDs) by a facile one-step hydrothermal approach. The localized surface plasmon resonance (LSPR) properties were achieved by oxygen vacancy engineered $WO_3 \cdot H_2O$ (dWO_3•H_2O), which could greatly extend the light absorption from visible light to near-infrared light. Moreover, by coupling with N-GQDs, the as-fabricated heterojunction (dWO_3•H_2O@N-GQD) provided a much enhanced photoelectric response due to the efficient charge transfer. By conjugation with *E.coli* O157:H7 aptamer, a novel PEC aptasensor based on dWO_3•H_2O@N-GQD heterojunction was fabricated with a high sensitivity for detection of *E.coli* O157:H7. The limit of detection (LOD) of this PEC aptasensor is 0.05 CFU/mL with a linear detection range from 0.1 to 10^4 CFU/mL. Moreover, high reproducibility and good accuracy could also be achieved for analysis in milk samples. This work could provide a promising platform for the development of PEC bioanalysis and offer an insight into the non-metallic plasmonic materials based heterojunctions for high-performances PEC biosensing.

Keywords: Tungsten oxide hydrate nanosheets (WO_3); Nitrogen doped graphene quantum dots (N-GQDs); Oxygen vacancy; Plasmonic; Photoelectrochemical (PEC) biosensing

1. Introduction

Escherichia coli (*E.coli*) is a common food-borne pathogen which can be found in human intestine and the polluted food or water (Giovanni et al., 2015; Zhou et al., 2018a). As one of the most harmful bacterium related to food-borne diseases, *E. coli* O157:H7 can cause the injury and pathological change in the gastrointestinal tract and urinary systems, leading to serious diseases such as bloody diarrhea, hemolytic uremic syndrome, and even death (Hao et al., 2017). The infectious dose of *E. coli* O157:H7 is as low as 10 CFU/mL (Rahal et al., 2012). So it is important to sensitively detect the presence of *E.coli* O157:H7 before it enters the body to cause a serious outbreak. At present, the common methods for detection of *E. coli* O157:H7 mainly include polymerase chain reaction (PCR), enzyme-linked immune-sorbent assay and culture plating method (Kim et al., 2014; Zeng et al., 2016; Wang et al., 2017). Although these methods are reliable and accurate, they are either time-consuming or require expensive equipment, which cannot satisfy the demands from clinical diagnosis and food safety monitoring (Hao et al., 2017). Therefore, it is important to develop a rapid, simple, sensitive and specific method for *E.coli* O157:H7 detection.

Biosensors have been developed for rapid and sensitive detection of *E. coli* O157:H7 including surface acoustic wave (SAW) (Lamanna et al., 2020), surface plasma resonance (SPR) (Vaisocherová-Lísalová et al., 2016), and electrochemical biosensors (Chan et al., 2013; Tian et al., 2016). Developing novel ultrasensitive biosensing technique for detecting *E. coli* O157:H7 is always of high demand. Photoelectrochemical (PEC) sensing is an innovative method that integrates electrochemistry with photochemistry, which has attracted great attention owing to its exquisite merits, including high sensitivity, robustness, low cost and simple instrumentation (Zhao et al., 2015; Zang et al., 2017). Moreover, such sensing systems have been widely used in various applications including food security analysis, environmental

monitoring, and clinical early diagnosis (Zhao et al., 2015; Zhao et al., 2016; Zhou et al., 2018b). In principle, the PEC sensing system is a distinctive signal-transduction pathway in which the photoactive materials can be excited by light of appropriate wavelength (Ruan et al., 2017; Jiang et al., 2019). Generally, widening the photoabsorption range and engineering the interfacial charge transfer are two promising strategies to improve exciton generation, achieve fast response, and enhance signal intensity for fabricating high-performances PEC biosensors.

Plasmonic nanostructures with fascinating localized surface plasmon resonance (LSPR) properties have drawn great interest in the research field of solar energy conversion because they have tremendous potential to harvest abundant low-energy photons from sunlight (Zhang et al., 2018; Iliev, V. et al., 2018; Prusty et al., 2020). Noble-metal nanoparticles, such as Au, Ag, and Cu, have been applied to extend light-absorption range based on their sharp plasmon resonance at short-wavelengths. However, the narrow light absorption region and high cost limit their wider application. With the rapid development of semiconductor-related nanoscience, the LSPR phenomenon has also been observed in the semiconductor nanomaterials, including WO_3, TiO_2, Cu_2O, MoO_3 et al (Prusty et al., 2020; Purbarani et al, 2019; Ke et al., 2016; Pareek et al., 2017). In contrast to the conventional noble metals, the excess free carriers on the surface of the vacancy-rich semiconductor nanoparticles could be induced by the incident light and cause collective oscillation, resulting in robust and broad light absorption. Among various semiconductors, tungsten oxides (WO_{3-x}) based nanomaterial with abundant oxygen vacancies have attracted much interest due to its facile synthesis and intense LSPR in visible and near-infrared region (Mirfasih et al., 2017; Prusty et al., 2020). Moreover, WO_{3-x} based nanomaterials possess a higher mobility (~12 cm^2 V^{-1} S^{-1}) during electron transfer which is beneficial for charge separation. What's more, oxygen vacancies in the WO_{3-x} based nanomaterials not only have a critical effect on the electronic and physicochemical properties such as electronic band structures and optical absorption, but also can serve as electron donors

which facilitate the charge transport (Mirfasih et al., 2017; Zhang et al., 2018).

Recently, two-dimensional oxygen vacancies engineered tungsten oxide hydrate nanosheets ($dWO_3 \bullet H_2O$) are anticipated to inspire novel research due to their unique optical and electrical properties (Li et al., 2014; Zhou et al., 2015; Guan et al., 2018). However, such nanomaterial still suffers from the high recombination rate of the photogenerated electron-hole pairs, which is a common problem in photoactive materials used in PEC sensors (Li et al., 2014). Semiconductor-based heterojunctions have emerged as one of important strategies for engineering the interfacial charge transfer. It is worth noting that the layered heterojunction composed of two-dimensional materials has attracted widespread attention due to the well-defined heterostructure, and can be easily assembled with other nanomaterials through facile wet chemical methods. Nitrogen-doped graphene quantum dot (N-GQD), as a kind of graphene-based materials, has been attracting great attention in various optoelectronic applications owing to its excellent photoelectric performance (Yeh et al., 2014). The coupling of N-GQDs with semiconductor materials could improve electrical conductivity, enhance charge transfer, and obtain longer charge carriers lifetime (Yin et al., 2016; Jiang et al., 2017). In this regard, the coupling of nonmetallic plasmonic two-dimensional WO_{3-x} based nanomaterials with N-GQDs may greatly enhance charge transfer and have an excellent PEC performance for biosensing. Until now, there is no report about heterostructure of WO_{3-x} and N-GQDs and its related biosensing applications.

In this paper, we have developed a novel PEC biosensor for *E.coli* O157:H7 detection based on plasmonic enhancement of oxygen vacancy-engineered tungsten oxide hydrate nanosheets ($dWO_3 \bullet H_2O$) coupling with N-GQDs. Such $dWO_3 \bullet H_2O$@N-GQDs heterostructures have broad photoabsorption from visible light to near-infrared light, and exhibit enhanced photocurrent intensity by efficient charge transfer. With the assistance of *E.coli* O157:H7

aptamer, our fabricated PEC sensor displayed good performance including wide linear detection range, rapid response, high stability and good selectivity with an ultralow limit of detection around 0.05 CFU/mL. This work provided an insight into the development of novel high-performance photoactive materials-based PEC biosensors for ultrasensitive detection of food-borne pathogens.

2. Experimental section

2.1 Reagents

Concentrated hydrochloric acid (HCl), concentrated nitric acid (HNO_3), sodium chloride (NaCl), potassium chloride (KCl), magnesium chloride ($MgCl_2$), Ethylene Diamine Tetraacetic Acid (EDTA), $Na_2WO_4 \bullet 2H_2O$, citric acid (CA) and glucose were purchased from Sigma-Aldrich, Inc. The N-GQDs were prepared by an easy reflux approach according to our previous work (Yin et al., 2016; Jiang et al., 2017). *E.coli* O157:H7 aptamer was purchased from Sangon Biotech Co., Ltd (Shanghai, China) with the following sequence (5' to 3'): 5'-GCAATGGTACGGTACTTCCCCATGAGTGTTGTGAAATGTTGGGACACTAGGTGGC ATAGAGCCGCAAAAGTGCACGCTACTTTGCTAA-3' (Guo et al., 2016; Hua et al., 2018) . Aptamer stock solutions were prepared with 50 mM Tris-HCl buffer (pH 7.4, containing 0.1 M NaCl, 0.2 M KCl, 5.0 mM $MgCl_2$ and 1.0 mM EDTA) and kept frozen in dark. 0.1 M KCl solution with 5 mM $[Fe(CN)_6]^{3-/4-}$ was utilized as the electrolyte for the electrochemical impedance spectra (EIS) characterization. 0.1 M phosphate-buffered saline solution (PBS) was employed as the supporting electrolyte during the whole process of PEC detection, which was a mixed solution of 0.1M NaH_2PO_4 and Na_2HPO_4. The pH value of PBS solution was adjusted to 7 by 0.1 M NaOH or HCl solution. All the solutions were processed with ultrapure water and the chemicals were all analytical reagent grade.

2.2 Apparatus

The morphologies of the samples were observed via transmission electron microscopy (TEM, Hitach H800, Japan) and scanning electron microscopy (SEM, JEOL JSM-6700, Japan) equipped with an energy-dispersive spectroscopy (EDS, Oxford Inca Energy 400, UK). Crystal structure identification was performed using a power X-ray diffraction spectroscopy (XRD, Bruker D8 ADVANCE diffractometer, Germany) with Cu-K radiation. X-ray photoelectron spectroscopy (XPS) was performed on a Thermo VG Scientific ESCALAB 250 spectrometer using a Mg K radiator. UV-vis diffuse reflectance spectrum was obtained with an UV-2450 spectro-photometer (Shimadzu Corporation, Japan) using $BaSO_4$ as the reference. The photoluminescence (PL) spectra were measured using a PerkinElmer fluorescence spectrometer (FL 6500). Photoelectrochemical (PEC) current measurement was conducted by a CHI 660E electrochemical workstation (Shanghai Chenhua Instrument Co. Ltd., China) at room temperature, which was connected to a conventional three-electrode cell using ITO electrode as a working electrode, saturated calomel electrode (SCE) as a reference electrode, and Pt wire as a counter electrode. All the PEC measurements were carried out in 0.1 M PBS solution and a 500 W Xe lamp (CHF-XM35-500W, Beijing Changtuo) was utilized as the light source with an intensity of 100 mW cm^{-2}. Current-time (I-t) method was used for the whole PEC experiments. The distance between the working electrode and visible light was fixed at 10 cm.

2.3 Bacteria culture

E. coli was recovered and cultured in Luria-Bertani broth (LB) medium at 37 ºC with shaking at 250 rpm overnight. After reaching stationary phase, *E. coli* culture solution (10 mL)

was centrifuged (5000 rpm, 10 min) and washed with PBS to obtain *E. coli* cells. Finally, *E. coli* were suspended in PBS to obtain *E. coli* stock solution at concentrations from 0 to 10^4 CFU/mL (colony-forming units per milliliter) for further experiments.

2.4 Preparation of photoactive nanocomposite material

The d$WO_3 \cdot H_2O$/N-GQDs nanocomposites were synthesized by a one-pot hydrothermal method. Firstly, 0.5 mM $Na_2WO_4 \bullet 2H_2O$, 0.75 mM CA, 0.5 mM glucose and a certain amount of N-GQDs were mixed with 15 mL ultrapure water to obtain a transparent solution under stirring at room temperature. After 1.5 mL 6 M HCl was added, the mixture was kept stirring for 30 minutes. Finally, the mixture solution was poured into 25 mL Teflon-lined autoclave and then heated at a temperature of 120 ℃ for 24 hours. After being naturally cooled to room temperature, the supernatant was filtered, and the precipitate was collected. The collected precipitate was washed by ethanol and water separately for at least 4 times. Then, the resultant precipitate was gathered and dried in an oven at 60 ^{0}C. The d$WO_3 \cdot H_2O$/N-GQDs composites with different N-GQDs amount were prepared by simply adjusting the ratio of N-GQDs proportion (1%, 2%, 4%, 5%, and 7%) during the synthesis process. For comparison, defect-free $WO_3 \bullet H_2O$/N-GQDs were prepared in the same way except for the addition of glucose. Furthermore, d$WO_3 \bullet H_2O$ and defect-free $WO_3 \bullet H_2O$ were synthesized in the same way except for the addition of N-GQDs and glucose.

2.5 Fabrication of PEC aptasensor for detection of E. coli O157:H7

Firstly, NaOH solution (1 M), ultrapure water and ethanol were applied respectively to clean the ITO pristine electrodes. The 2 mg mL^{-1} d$WO_3 \cdot H_2O$/N-GQDs suspension was obtained by

scattering 2 mg $dWO_3 \bullet H_2O$/N-GQDs nanocomposites in 1 mL DMF and vibrated with ultrasound until uniform. After dropping the suspension onto the planned sensing area (5 mm×5 mm) on the ITO electrode, the electrodes with the suspension were stored in an oven at 120 °C for several hours in order to strengthen the adhesion between electrode interface and $dWO_3 \bullet H_2O$/N-GQDs. After that, ITO/$dWO_3 \bullet H_2O$/N-GQDs coated electrodes were obtained. ITO/$WO_3 \bullet H_2O$/N-GQDs electrode, ITO/$WO_3 \bullet H_2O$ electrode and ITO/$dWO_3 \bullet H_2O$ electrode were obtained using a similar procedure.

For the fabrication of the PEC aptasensor for *E.coli* O157:H7 detection, 20 μL of 1 μM *E.coli* O157:H7 aptamer was dropped on the sensing area of ITO/$dWO_3 \cdot H_2O$/N-GQDs-coated ITO electrodes. After incubating with aptamer solution, the electrodes were dried for 6 hours in the air to enhance the adhesion. Thus, ITO/$dWO_3 \cdot H_2O$/N-GQDs/aptamer electrodes were fabricated successfully. Finally, in order to block the remaining active sites, 20 μL 1% BSA was dropped on the electrode and the unattached BSA was washed away by PBS buffer solution after 1 hour coating. During the PEC sensing process, 20 μL of *E.coli* O157:H7 solution with different concentrations was casted on the PEC aptasensor for incubation of 30 minutes. Finally, unattached *E.coli* O157:H7 was washed away with PBS solution before PEC detection.

A real sample test in milk was performed in order to confirm the practicability of this PEC sensing device. Milk from the local market (Wellcome supermarket, Hong Kong, China) was firstly mixed with PBS buffer solution (pH=7.0) with a volume ratio of 1:4. The solution was ultrasonically vibrated and then shaken for 10 minutes, respectively. The prepared samples were then spiked with *E.coli* O157:H7 with a series of concentrations from 1 to 1000 CFU/mL.

3. Results and Discussion

3.1 Characterizations of the photoactive nanocomposite material

The morphology of $dWO_3 \cdot H_2O$, N-GQDs and $dWO_3 \cdot H_2O$/N-GQDs nanocomposite is characterized by SEM and TEM. The SEM and TEM images of $dWO_3 \cdot H_2O$ show 2D nanostructure with the size of 100~150 nm (Fig. S1a, S1b). N-GQDs show good water dispersion with a small size of 3~5 nm (Fig. S1c). SEM image reveals that the nanocomposites of $dWO_3 \cdot H_2O$/N-GQDs do not show obvious morphology change after doping of N-GQDs compared with $dWO_3 \cdot H_2O$ (Fig. 1A). Moreover, the detailed structure of the nanocomposite materials is further investigated by TEM. As shown in Fig. S2, N-GQDs are randomly dispersed on the surface of $dWO_3 \cdot H_2O$ nanosheets and high-resolution transmission electron microscopy (HRTEM) confirms that small size N-GQDs attach onto $dWO_3 \bullet H_2O$ with a size of roughly around 3~5 nm. N-GQD shows a d-spacing of 0.20 nm corresponding to the (002) lattice fringe (Inlet of Fig. S2).

The crystal phase of the $dWO_3 \bullet H_2O$@N-GQDs nanocomposite is also investigated by the powder XRD analysis. The diffraction pattern of $dWO_3 \cdot H_2O$/N-GQDs nanocomposite shows typical peaks at 2θ equal to 16.5^0, 23.8^0, 25.7^0, 30.5^0, 33.4^0, 34.2^0, 35.0^0, 37.7^0, 38.9^0, 45.9^0, 49.2^0, 52.8^0, 54.3^0, 56.3^0, 62.8^0 and 66.2^0, which match well with orthorhombic structure of the $WO_3 \bullet H_2O$ phase (JCPDS no. 43-0679), respectively (Zhang et al., 2016; Zhang et al., 2017). The XRD results clearly present the existence of $WO_3 \bullet H_2O$ in $dWO_3 \bullet H_2O$/N-GQDs nanocomposites. No characteristic diffraction peaks of N-GQDs are observed in XRD spectrum because of its lower loading content and weak crystallization, which also implies the good dispersion of very small N-GQDs on the surface of $WO_3 \bullet H_2O$ nanosheet. The element composition on the surface of the nanocomposite $dWO_3 \cdot H_2O$/N-GQDs is further explored by XPS spectra (Fig. 1C). XPS survey spectra of the hybrid nanocomposite show the existence of

W, C, N, O elements. Furthermore, the high resolution XPS of N_{1s} (inset of Fig. 1C) shows four peaks corresponding to amine nitrogen, graphitic nitrogen, pyridine nitrogen, and pyrrolic nitrogen in the nanocomposite, respectively, which further confirms the co-existence of $dWO_3 \cdot H_2O$ and N-GQDs in the nanocomposites.

To identify the defects in nanosheets, room-temperature electron spin resonance (ESR) spectroscopy and UV–vis diffuse reflectance spectroscopy (UV-DRS) are both used to characterize the defective sample with non-defective $WO_3 \bullet H_2O$/N-GQDs as the reference. As shown in Fig. 1D, $dWO_3 \bullet H_2O$ nanosheets exhibits a significant ESR signal at g = 2.002 that could be attributed to the electron trapping at oxygen vacancies (Zhang et al., 2016). In addition, two characteristic peaks at the binding energies of 35.8 eV and 38.0 eV could be well assigned to the 4f 7/2 and 4f 5/2 for W^{6+}, respectively, in the high-resolution W 4f XPS spectra of $WO_3 \bullet H_2O$/N-GQDs (Fig. S3). In comparison, the peaks of W 4f 7/2 and 4f 5/2 for $dWO_3 \bullet H_2O$/N-GQDs are obviously shifted to 35.4 eV and 37.6 eV, respectively. The lower binding energies indicated the increase of electron density in W atoms, which further verifies the existence of oxygen vacancies (Zhang et al., 2017). Such oxygen vacancies might be beneficial for improving the light absorption and charge transfer. Moreover, the UV-DRS spectra show the influence of introduction of oxygen vacancy and N-GQDs on photo-absorption capability of nanocomposite (Fig. S4). Compared to $WO_3 \bullet H_2O$ (curve a), $dWO_3 \bullet H_2O$ (curve b) and $WO_3 \cdot H_2O$/N-GQDs nanocomposite (curve c) exhibit roughly the same trend of the curve but with obviously higher light absorption. Especially, after introducing both N-GQDs and oxygen vacancy due to defects, the reflectance of the material $dWO_3 \cdot H_2O$/N-GQDs (curve d) increases in both visible-light range and near-infrared range. This $dWO_3 \cdot H_2O$/N-GQDs nanocomposite integrates both broad visible absorption bands of N-GQDs and remarkable near-infrared light harvesting caused by defects introduction. Based on

the Tauc plot, the band gaps of $WO_3 \cdot H_2O$ and $dWO_3 \cdot H_2O$ are 2.70 eV and 2.52 eV, respectively, which show the shortening of band gap (Fig. S5). The dramatic increase of near-infrared absorption might be attributed to the shortened band gap due to the upshifting of valence band and the defect below the conduction band (Zhang et al., 2016; Zhang et al., 2017).

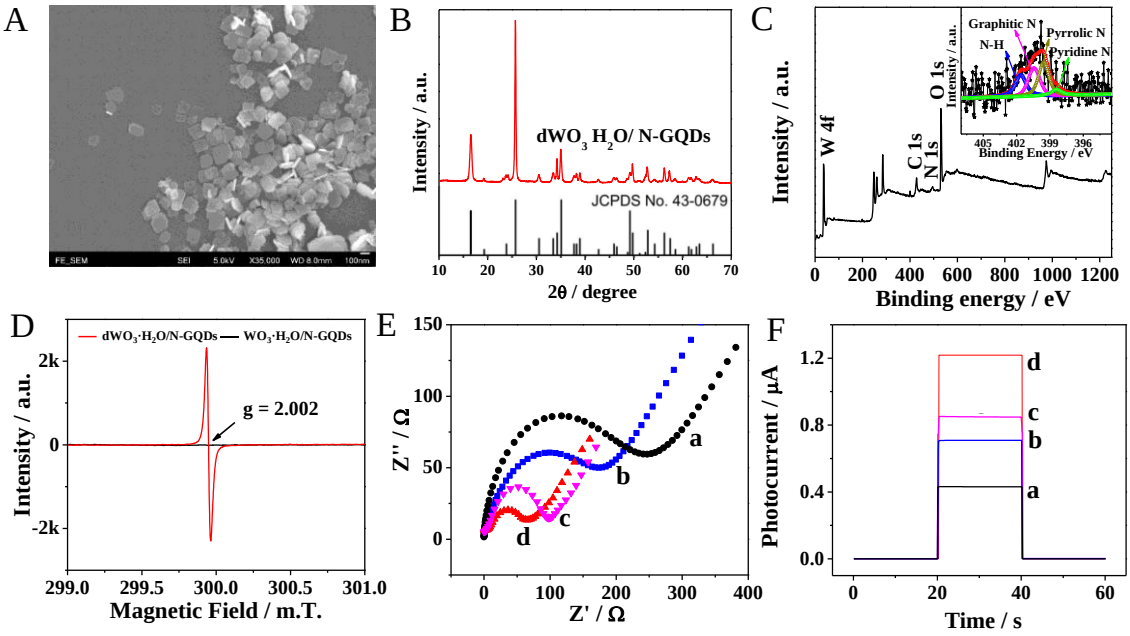

Fig.1 (A) SEM image of $dWO_3 \bullet H_2O$/N-GQDs nanocomposite. (B) XRD patterns of JCPDS no. 43-0679 and $dWO_3 \bullet H_2O$/N-GQDs nanocomposite. (C) XPS survey spectra of $dWO_3 \bullet H_2O$/N-GQDs nanocomposite. Inset: high resolution XPS spectra of the N_{1s} region of the nanocomposites. (D) ESR survey spectra of nanocomposite $WO_3 \bullet H_2O$/N-GQDs with and without oxygen vacancies. (E) EIS Nyquist plots and (F) photocurrents of ITO electrodes coated with $WO_3 \bullet H_2O$ (curve a), $dWO_3 \bullet H_2O$ (curve b), $WO_3 \bullet H_2O$/N-GQDs (curve c), and $dWO_3 \bullet H_2O$/N-GQDs (curve d)

3.2 The EIS properties and PEC performance of the photoactive nano-composite

To explore the effect of oxygen vacancies and N-GQDs on the nanocomposites, the

electrochemical impedance spectroscopy (EIS) and PEC characterization of ITO electrodes modified with different samples are measured. Fig. 1E displays the EIS plot of $WO_3 \bullet H_2O$ (curve a), $dWO_3 \bullet H_2O$ (curve b), $WO_3 \bullet H_2O$/N-GQDs (curve c), and $dWO_3 \bullet H_2O$/N-GQDs (curve d). As we all know, the semicircle on the plot represents the resistance in electron transfer (R_{et}). The smaller the diameter of the semicircle, the lower the charge transfer resistance. Obviously, the nanocomposites of $dWO_3 \bullet H_2O$/N-GQDs possesses the smallest semicircle diameter, indicating oxygen vacancy and N-GQDs act important roles in efficiently facilitating electron transfer. Moreover, it can be observed that curve c has a lower R_{et} than curve b, which indicates the strategy of coupling N-GQDs has higher effects than that of oxygen vacancy on facilitating charge transfer.

To further explore the effects of oxygen vacancies and N-GQDs on the photoelectric response, the transient photocurrents of ITO electrodes modified with different materials were recorded. As shown in Fig. 1F, the ITO electrode modified with $WO_3 \bullet H_2O$ (curve a) only gains lowest photocurrent (~0.45 μA) among all the modified electrodes. On the contrary, the ITO electrode that modified with $dWO_3 \cdot H_2O$ as well as N-GQDs (curve d) shows the highest photocurrent (~1.2 μA), which is nearly twice times higher than that of N-GQDs and oxygen vacancy only, indicating the important role of these two elements in improving the PEC performance. In addition, curve c presents higher photocurrent than curve b, substantiating the same result of EIS analysis that coupling N-GQDs is more efficient in facilitating the charge transfer than introducing oxygen vacancy.

3.3 Mechanism and fabrication of PEC aptasensor

Fig. 2A shows the whole construction and fabrication process of the PEC aptasensor based on $dWO_3 \bullet H_2O$/N-GQDs. Upon irradiation, the photoactive nanocomposite is excited and the

photogenerated electrons then transfer from the valance band (VB) to conduction band (CB). Furthermore, the electrons further transfer onto the ITO electrode and the holes are supplied by the donors in the electrolyte. The hybrid photoactive material $dWO_3 \cdot H_2O$/N-GQDs, prepared by a facile one-step hydrothermal synthesis method can effectively enhance photocurrents and achieve superior PEC performance due to the combination of N-GQDs and WO_3 with both surface defects and lattice water. On one hand, the Brønsted acid sites from lattice water can enhance adsorption of alkaline amine molecules and strengthen the internal binding of nanocomposite. In this system, the aptamer was immobilized onto the surface of $dWO_3 \bullet H_2O$/N-GQDs via π–π stacking interaction between aromatic ring of N-GQDs and nucleobases. The high surface-to-volume ratio and π-conjugated structure of N-GQDs provides an excellent platform for aptamer immobilization via π–π stacking interaction. (Liu et al., 2015; You et al., 2019). When *E.coli* aptamers are immobilized on ITO electrodes modified with $dWO_3 \bullet H_2O$/N-GQDs, the current signal will decrease as a result of steric hindrance, i.e. the electron transfer is hindered by the changed internal structure. Moreover, capturing target *E.coli* on aptamer-modified ITO electrodes will further decrease the photocurrent signal for the same reason of steric hindrance.

After the ITO electrode was modified with the nanocomposite and followed by conjugation with aptamer, the PEC aptasensor was fabricated successfully. Besides, BSA was introduced into the system in order to block the remained unspecific binding sites on the surface of nanocomposite (Guo et al., 2016; Hao et al., 2017; Hua et al., 2018). The stepwise construction process of PEC aptasensor system and its working capability can be monitored and characterized by EIS analysis and photocurrent measurement. EIS analysis shows that the R_{et} significantly increases after coating with aptamer onto the electrode (curve b) (Fig. 2B). The larger curve diameter after aptamer conjugation (curve b) is attributed to the electrostatic repulsion effect between aptamers and negative charges from the $[Fe(CN)_6]^{3-/4}$, which can

directly affect R_{et}. Likewise, the further increase of R_{et} after BSA blocking is due to the further hindering of transfer of $[Fe(CN)_6]^{3-/4-}$ onto ITO electrodes. When target *E.coli* O157:H7 were captured by aptamers on ITO electrodes (curve d), the further increase of R_{et} due to a larger steric hindrance was observed due to the similar reason.

The change of PEC photocurrents can further manifest the stepwise assembly of the PEC sensor for *E.coli* O157:H7 detection. As shown in Fig. 2C, the conjugation of aptamer and BSA blocking subsequently lowers the photocurrent (curve a→c) due to the increased hindrance effects on interfacial electrolyte transfer process of ITO electrodes. The capturing of *E.coli* O157:H7 forms a complex layer of $dWO_3 \cdot H_2O$/N-GQDs/aptamer/*E.coli*, which dramatically decreases the photocurrent (curve d). The change of surface structure and poor conductivity of the complex layer on the electrode result in the larger steric hindrance, which hamper the transfer of electron donor to electrode surface and lead to the decrease of the photocurrent. Therefore, by monitoring the photocurrent change, *E.coli* O157:H7 in the sample can be detected quantitatively.

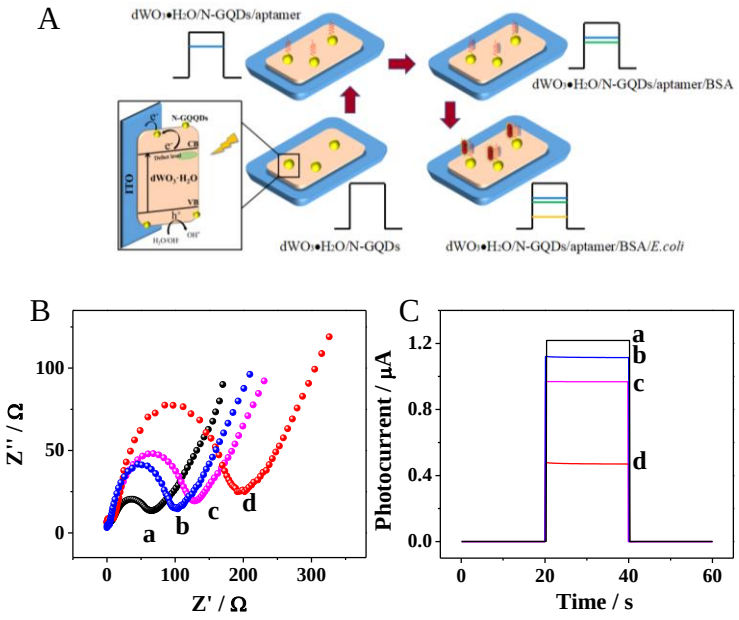

Fig. 2 (A) The fabrication process of the PEC aptasensor for detection of *E.coil* O157:H7. (B)

EIS and (C) PEC characterization of the PEC aptasensor during the fabrication process. Here, curve a is for original ITO electrode modified with $dWO_3 \bullet H_2O$/N-GQDs nanocomposite; curve b is after aptamer conjugation on ITO electrodes modified with nanocomposite; curve c is after BSA blocking on aptamer-conjugated ITO electrodes modified with nanocomposite; curve d is for *E.coil* O157:H7 capturing on aptamer-conjugated ITO electrodes modified with nanocomposite after BSA blocking.

3.4 Optimization of experimental conditions of $dWO_3 \cdot H_2O$/N-GQDs modified electrode

In order to get a better PEC performance, the experimental parameters should be optimized. In this paper, the optimization of buffer pH value, N-GQDs concentration, aptamer concentration and binding time were performed. For investigating the effect of pH value of electrolyte on the PEC response, the photocurrents of the nanocomposites-modified electrodes were measured under different pH values of PBS from 5 to 9. The photocurrent reaches the maximum when pH value of buffer solution equals to 7 and then decreases with the further increase of pH value, which matches the optimal growth pH value of *E.coli* (Fig. 3A). Therefore, pH = 7 is considered as the optimal pH value for PEC sensing and utilized in the following experiment. Moreover, it is known that the intensity of PEC photo-response is strongly dependent on the components in the photoactive nanocomposite. Therefore, the effect of N-GQDs ratio in the nanocomposite on the photo-response of PEC sensor was studied. The photocurrent increased with the increasing of ratio of N-GQDs in the nanocomposite and reached a peak when the proportion of N-GQDs was 4% (Fig. 3B). Nevertheless, with the further increasing of N-GQDs ratio, the photocurrent decreased. The photoluminescence (PL) spectra have been widely used to reveal the charge transfer, migration and recombination processes in photoactive materials (Sari et al., 2019; Sari et al., 2020). As shown in Fig. S6,

compared with pure $WO_3 \bullet H_2O$ (curve a) and pure dWO_3H_2O (curve c), the doping of NGQDs leads to weaker PL intensities of $WO_3 \bullet H_2O$/NGQDs (curve b) and $dWO_3 \bullet H_2O$/NGQDs (curve d), indicating that both phase junction and oxygen vacancy can reduce recombination of photogenerated electron-hole pairs. Moreover, $dWO_3 \bullet H_2O$/NGQDs (curve d) shows the lowest PL signal, indicating that the coupling of phase junction and oxygen vacancy are beneficial to the charge transfer (Sun et al., 2017; Li et al., 2017). This phenomenon might be attributed to the excessive N-GQDs, which drained the recombination of photogenerated electron-hole pairs and then resulted in the decline of photocurrents. Consequently, the optimal ratio of N-GQDs in the nanocomposite was confirmed to be 4% which was applied in the following experiment. Besides the conditions above, the binding time of *E.coli* O157:H7 with aptamer on the ITO electrodes can also affect the PEC performance. It takes certain time for *E.coli* to fully interact with the aptamer. A false negative result could be obtained if the *E.coli* have not been incubated for enough time. Upon addition of *E.coli* O157:H7 sample, the photocurrent decreases at the around first 30 minutes and then reaches a stable plateau around 40 minutes (Fig. 3C). The result indicates the optimal detection time for *E.coli* is 40 minutes which is employed in the follow-up study.

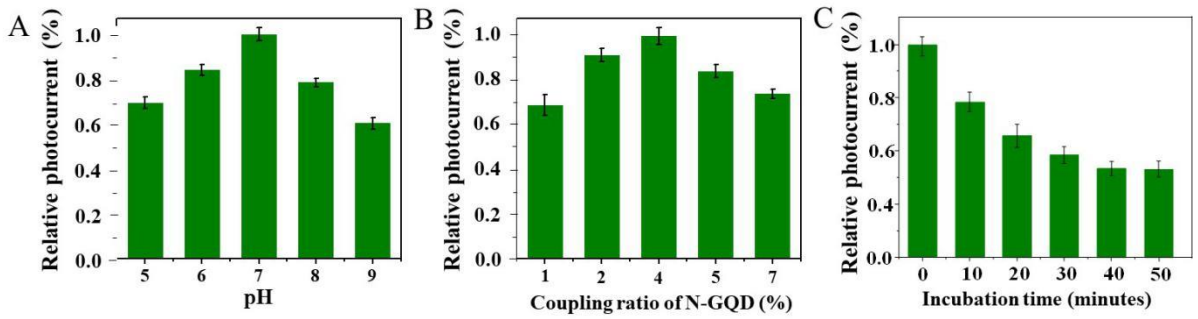

Fig. 3 (A) Effect of pH, (B) concentration of N-GQDs, and (C) binding time on the photocurrent intensity of the PEC sensor.

3.5 Ultrasensetivity and feasibility of PEC aptasensor for E.coli detection

After optimization of the detection parameters, the established PEC aptamer biosensor is then used for quantitative *E.coli* detection. Fig. 4A shows the PEC photo-response of $dWO_3 \cdot H_2O$/N-GQDs/aptamer electrodes toward the different concentrations of *E.coli*. Under the optimal condition, the intensity of photocurrent decreases with the increasing of the *E.coli* O157:H7 concentration, which is attributed to the steric hindrances caused by capturing more *E.coli* in the PEC system. The corresponding photocurrent is linearly correlated to the logarithm of *E.coli* O157:H7 concentration, ranging from 0.1 to 10^4 CFU/mL. When the concentration of *E.coli* is above 10^4 CFU/mL, an obvious saturation plateau was observed (Fig. 4B). The limited of detection (LOD) is estimated to be 0.05 CFU/mL by the control signal plus 3 times of the standard deviation, representing a higher sensitivity than those of other *E.coli* detection methods (Zhou et al., 2018a; Hao et al., 2017; Kim et al., 2014; Zeng et al., 2016).

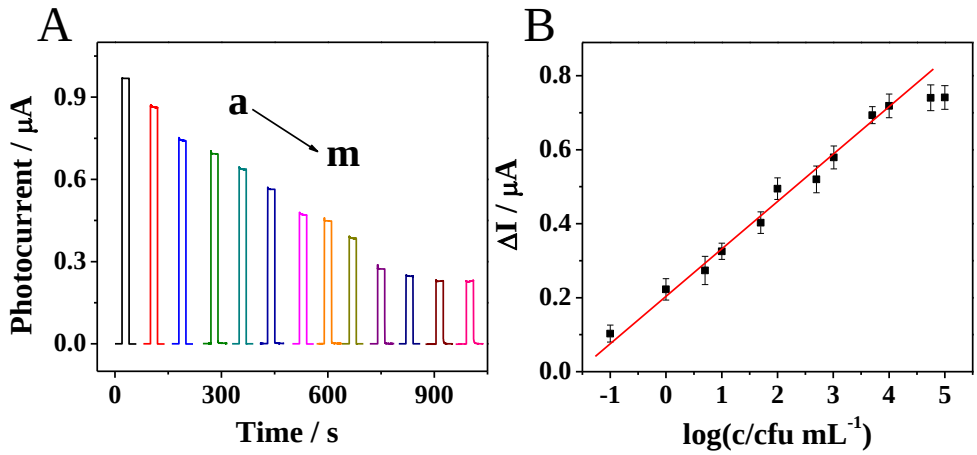

Fig. 4 (A) Photocurrent responses of the PEC aptasensor upon addition of serial concentration of E.coli under the optimal conditions (from a to g: 0 to 10^5 CFU/mL). (B) The corresponding linear calibration curve for *E.coli* O157:H7determination.

To confirm the capability of the developed aptasensor in performing practical detection, the selectivity, stability and reproducibility research have been carried out. For the selectivity study, *E.coli* O157:H7, *Staphylococcus aureus (S.aureus)*, *staphylococcus lactis* and *staphylococci* with the same concentration of 10^4 CFU/mL are introduced in the electrodes modified with *E.coli* O157:H7 aptamers respectively. As shown in Fig. 5A, only *E.coli* O157:H7 could result in a significant PEC response, while no obvious photo-response was observed for other bacteria, demonstrating the specificity of this PEC aptamer sensor for *E.coli* O157:H7. In order to commercialize the PEC sensor into practical product, its stability should be evaluated. By measuring the photocurrent for over 500 s, the PEC photo-response has been recorded for 10 times (Fig. 5B). There is no obvious difference among these 10 photo-response, indicating the firm attachment of the photoactive nanocomposite and aptamer on the electrode which offer reliability and stability for long time detection.

In addition, the repeatability of the PEC aptasensor is also assessed through five $dWO_3 \cdot H_2O$/N-GQDs nanocomposites modified ITO electrodes. The PEC photo-response shows a relative standard deviation (RSD) in 4.5% among five electrodes. Meanwhile, measurement is also carried out on the same five electrodes that is incubated with *E.coli* O157:H7 with a concentration of 10^3 CFU/mL, which yields a RSD of 3.1%. Furthermore, the PEC aptasensor is evaluated by the photo-response performance of the $dWO_3 \cdot H_2O$/N-GQDs/aptamer-modified ITO electrodes which are stored for 2 weeks under 4ºC. No obvious change can be observed in the photo-response before and after store, suggesting the duration of validity of the PEC aptasensor can last for at least 2 weeks. All the results above demonstrate the good repeatability and stability of the PEC aptasensor.

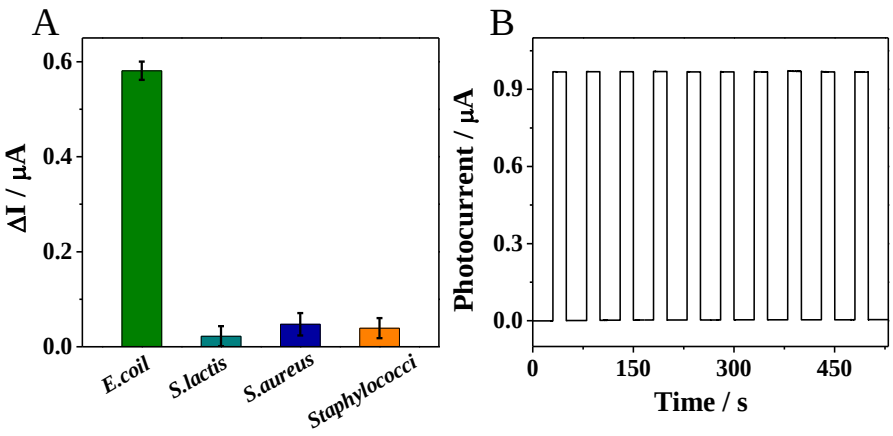

Fig. 5 (A) The selectivity and (B) stability of the PEC aptasensor.

3.6 Analysis of real samples

The proposed PEC aptasensor is also applied in real sample detection to evaluate the practical utility. The samples are prepared by milk sample that is spiked with different concentration of *E.coli* O157:H7. Three *E.coli* O157:H7 concentrations of 10, 10^2 and 10^3 CFU/mL are measured and the recovery rates are 4.7%, 3.9% and 5.8% respectively (Table 1). The high recovery rate manifests the accuracy and reliability of the PEC aptasensor as well as the potential application value in real sample detection. Moreover, real examples of milk spiked with *E.coli* O157:H7 with various concentrations have also been measured and quantified by a conventional plate count method to compare with the results of the aptasensor. As shown in Table 1, the results of the aptasensor match well with the results of the conventional plate count method, which demonstrate the feasibility of our sensors for real sample measurement. This PEC biosensor not only has ultrasensitivity, but also can satisfy nearly all demands in field detection, such as portability, short detection time and easy operation. It is of great practical application value for rapid detection of *E.coli* O157:H7 and owns a bright future in commercial application.

Table 1 Determination of *E.coli* O157:H7 in milk samples.

Sample	Spike (CFU/mL)	This method (CFU/mL)	Recovery (%)	RSD (%, n=3)	Plate count method (CFU/mL)
Milk (from local market)	10	9.8	98.0	4.7	9.7
	100	96.3	96.3	3.9	102.5
	1000	1054.0	105.4	5.8	976.2

4. Conclusion

In summary, a novel PEC aptasensor platform based on $dWO_3 \bullet H_2O$@N-GQDs nanocomposite is successfully fabricated for the rapid detection of *E.coli* O157:H7 with high sensitivity. By coupling $dWO_3 \cdot H_2O$ with N-GQDs via a one-pot hydrothermal method, the novel $dWO_3 \bullet H_2O$@N-GQDs photoactive nanocomposite material significantly enhances PEC photo-response as a result of restriction of the recombination of photogenerated electron-hole pair as well as acceleration of the charge transfer process in both visible light and NIR light regions. Furthermore, the PEC aptasensor provides a wide linear detection range (0.1 to 10^4 CFU/mL) with a high sensitivity (detect limit of 0.05 CFU/mL). Finally, this PEC aptasensor platform also has advantages of rapid response, good stability and repeatability, which can be widely applied in detection not only for *E.coli* O157:H7 but also many other pathogens.

CRedit authorship contribution statement

Ding Jiang: Experimental design, Tungsten oxide nanosheets synthesis, Photoelectrochemical measurement, Original draft, Data analysis. **Cuiqi Yang**: Bacteria

sensing, Data analysis, diagram drawing. **Yadi Fan**: N-GQD synthesis. **Hang-Mei Polly Leung**: Bacterial culture and counting. **Inthavong Kiao:** Review and editing. **Yu Zhang:** Nanomaterial characterization. **Zhiyang Li:** Review and editing. **Mo Yang**: Conceptualization, Recourses, Supervision, Final editing Funding acquisition.

Declaration of competing interest

The authors declare that they have no known competing financial interests or personal relationships that could have appeared to influence the work reported in this paper.

Acknowledgments

This work was supported by the National Natural Science Foundation of China (NSFC) (Grant Nos. 31771077 and 21904014), the Research Grants Council (RGC) of Hong Kong Collaborative Research Grant (C5011-19G), Innovation and Technology Fund, Guangdong-Hong Kong Cooperation Scheme (GHP-039-18GD), the Research Grants Council (RGC) of Hong Kong General Research Grant (152146/19E and 152108/18E), the Hong Kong Polytechnic University Internal Fund (G-YW2H and 1-ZE1E), the Natural Science Foundation of Jiangsu Province (BK20190928), and the Natural Science Foundation of the Jiangsu Higher Education Institutions of China (19KJB150003). This work was also supported by the University Research Facility in Life Sciences of the Hong Kong Polytechnic University.

References

Chan, K.Y., Ye, W.W., Zhang, Y., Xiao, L.D., Leung, P.H.M., Li, Y., Yang, M., 2013. Biosens.

Bioelectron. 41, 532-537.

Giovanni, M., Setyawati, M. I., Tay, C. Y., Qian, H., Kuan, W. S., Leong, D. T., 2015. Adv. Funct. Mater. 25, 3840-3846.

Guan, G. J., Wu, M. D., Cai, Y. Q., Liu, S. H., Cheng, Y., Tee, S. Y., Zhang, Y. W., Han, M. Y., 2018. Chem. Mater. 30, 5108-5115.

Guo, Y., Wang, Y., Liu, S., Yu, J.H., Wang, H.Z., Wang, Y.L., Huang, J.D., 2016. Biosens. Bioelectron. 75, 315-319.

Hao, N., Zhang, X., Zhou, Z., Hua, R., Zhang, Y., Liu, Q., Qian, J., Li, H. N., Wang, K., 2017. Biosens. Bioelectron. 97, 377-383.

Hua, R., Hao, N., Lu, J. W., Qian, J., Liu, Q., Li, H. N., Wang, K., 2018. Biosens. Bioelectron. 106, 57-63.

Iliev, V., Tomova, D., Bilyarska, L., 2018. J. Photochem. Photobiol., A 351, 69-77.

Jiang, D., Du, X. J., Liu, Q., Hao, N., Wang, K., 2019. Biosens. Bioelectron. 126, 463-469.

Jiang, D., Du, X. J., Zhou, L., Li, H. N., Wang, K., 2017. Anal. Chem. 89, 4525-4531.

Ke, C.R., Guo, G.S., Su, Y.H., Ting, J.M., 2016. Nanotechnology 27, 435405.

Kim, T. H., Park, J., Kim, C. J., Cho, Y. K., 2014. Anal. Chem. 86, 3841-3848.

Lamanna, L., Rizzi, F., Bhethanabotla, V.R., De Vittorio, M., 2020, Biosens. Bioelectron. 163, 112164

Li, Y.S., Tang, Z.L., Zhang, J.Y., Zhang, Z.T., 2017. Appl. Catal. B-Environ. 207, 207-217.

Li, W. J., Da, P. M., Zhang, Y. Y., Wang, Y. C., Lin, X., Gong, X. G., Zheng, G. F., 2014. ACS Nano 8, 11770-11777.

Liu, Y., Yan, K., Okoth, O.K., Zhang, J.D., 2015. Biosens. Bioelectron. 74, 1016-1021.

Mirfasih, M.H., Li, C.L., Tayyebi, A., Cao, Q., Yu, J., Delaunay, J.J. 2017. RSC Adv. 7, 26992-27000.

Pareek, A., Kim, H.G., Paik, P., Borse, P.H. 2017. J. Mater. Chem. A. 5, 1541-1547

Prusty, G., Lee, J.T., Seifert, S., Muhoberac, B.B., Sardar, R., 2020. J. Am. Chem. Soc. 142, 5938-5942

Purbarani, M.E., Sari, F.N.I., Ting, J.M., 2019. Surf. Coat. Technol. 378, 125073.

Rahal, E.A., Kazzi, N., Nassar, F.J., Matar, G.M., 2012. Front Cell Infect Microbiol. 2, 138.

Ruan, Y. F., Zhang, N., Zhu, Y. C., Zhao, W. W., Xu, J. J., Chen, H. Y., 2017. Anal. Chem. 89, 7869-7875

Sari, F.N.I., Lin, Q., Ting, J.M., 2019. Chem. Eng. J. 368, 784-794.

Sari, F.N.I., Yen, D.T.K., Ting, J.M., 2020. Appl. Surf. Sci. 533, 147506.

Sun, J., Guo, J., Ye, J., Song, B., Zhang, K., Bai, S., Luo, R., Li, D., Chen, A., 2017. J. Alloy Compd. 692, 876-884.

Tian, F., Lyu, J., Shi, J.Y., Tan, F., Yang, M. 2016. Sensors and Actuators B-Chemical 225, 312-318.

Wang, W., Zijlstra, R. T., Gänzle, M. G., 2017. BMC Microbiol. 17, 114.

Vaisocherova-Lisalova, H., Visova, I., Ermini, M.L., Springer, T., Song, X.C, Mrazek, J., Lamacova, J., Lynn, N.S., Sedivak, P., Homola, J., 2016. Biosens. Bioelectron. 80, 84-90.

Yeh, T. F.; Teng, C. Y.; Chen, S. J.; Teng, S., 2014. Adv. Mater. 26, 3297-3303.

Yin, Y. Y., Liu, Q., Jiang, D., Du, X. J., Qian, J., Mao, H. P., Wang, K., 2016. Carbon 96, 1157-

1165.

You, F.H., Zhu, M.Y., Ding, L.J., Xu, Y.H., Wang, K., 2019. Biosens. Bioelectron. 130, 230-235.

Zang, Y., Lei, J.P., Ju, H.X., 2017. Biosens. Bioelectron. 96, 8-16.

Zeng. Y., Wan. Y., Zhang D., 2016. Microchim. Acta 183, 741-748.

Zhang, H. Y., Tian, W. J., Li, Y. G., Sun, H. Q., Tade, M. O., Wang, S. B., 2018. J. Mater. Chem. A, 6, 6265-6272.

Zhang, N., Li, X.Y., Ye, H. C., Chen, S. M., Ju, H. X., Liu, D. B., Lin, Y., Ye, W.,Wang, C. M., Xu, Q., Zhu, J. F., Song, L., Jiang, J., Xiong, Y. J., 2016. J. Am. Chem. Soc. 138, 8928-8935.

Zhang, N., Li, X., Liu, Y., Long, R., Li, M., Chen, S., Xiong, Y., 2017. Small, 13, 1701354.

Zhao, W.W., Xu, J.J., Chen, H.Y., 2015. Chem. Soc. Rev. 44, 729-741.

Zhao, W.W., Xu, J.J., Chen, H.Y., 2016. TrAC-Trends Anal. Chem. 82, 307-315.

Zhou, C., Zou, H. M., Li, M., Sun, C. J., Ren, D. X., Li, Y. X., 2018a. Biosens. Bioelectron. 117, 347-353.

Zhou, P. S., Xu, Q., Li, H. X., Wang, Y., Yan, B., Zhou, Y. C., Chen, J. F., Zhang, J. N., Wang, K. X., 2015. Angew. Chem. 127, 15441-15445.

Zhou, Z. X., Zhang, Y. Y., Shen, Y. F., Liu, S. Q., Zhang, Y. J., 2018b. Chem. Soc. Rev. 47, 2298-2321.

Supporting Information

Ultra-sensitive photoelectrochemical aptamer biosensor for detecting E. coli O157:H7 based on nonmetallic plasmonic two-dimensional hydrated defective tungsten oxide nanosheets coupling with nitrogen-doped graphene quantum dots (dWO$_3$•H$_2$O@N-GQDs)

Ding Jiang,[a,b] Cuiqi Yang,[a] Yadi Fan,[a] Hang-Mei Polly Leung,[c] Inthavong Kiao,[d] Yu Zhang,[d] Zhiyang Li,[e] Mo Yang [a,*]

a Department of Biomedical Engineering, The Hong Kong Polytechnic University, Hong Kong, P. R. China

b Jiangsu Key Laboratory of Advanced Catalytic Materials and Technology, School of Petrochemical Engineering, Changzhou University, Changzhou 213164, China

[c] Department of Health Technology and Informatics, The Hong Kong Polytechnic University, Hong Kong, P. R. China

[d]Department of Mechanical and Automotive Engineering, Royal Melbourne Institute of Technology University, Melbourne, Victoria 3000, Australia

[e] Department of Clinical Laboratory, the Affiliated Drum Tower Hospital of Nanjing University Medical School, Nanjing 210008, China

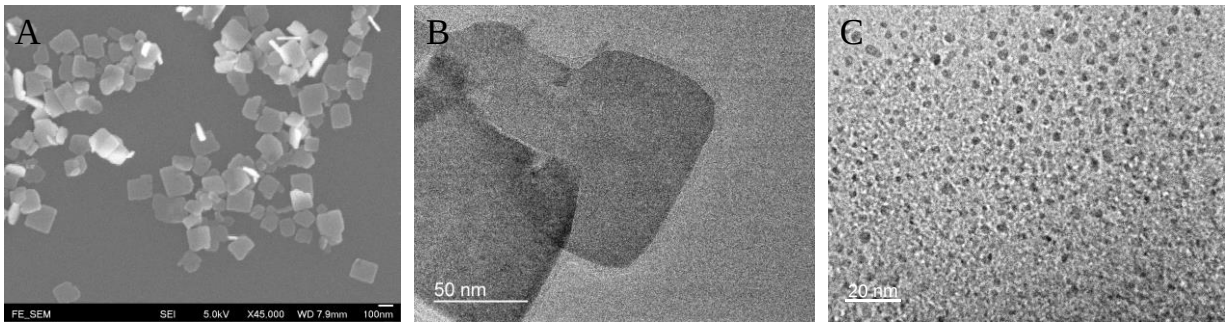

Fig. S1 SEM image (A) and TEM image (B) of dWO_3*H_2O. (C) TEM image of N-GQDs.

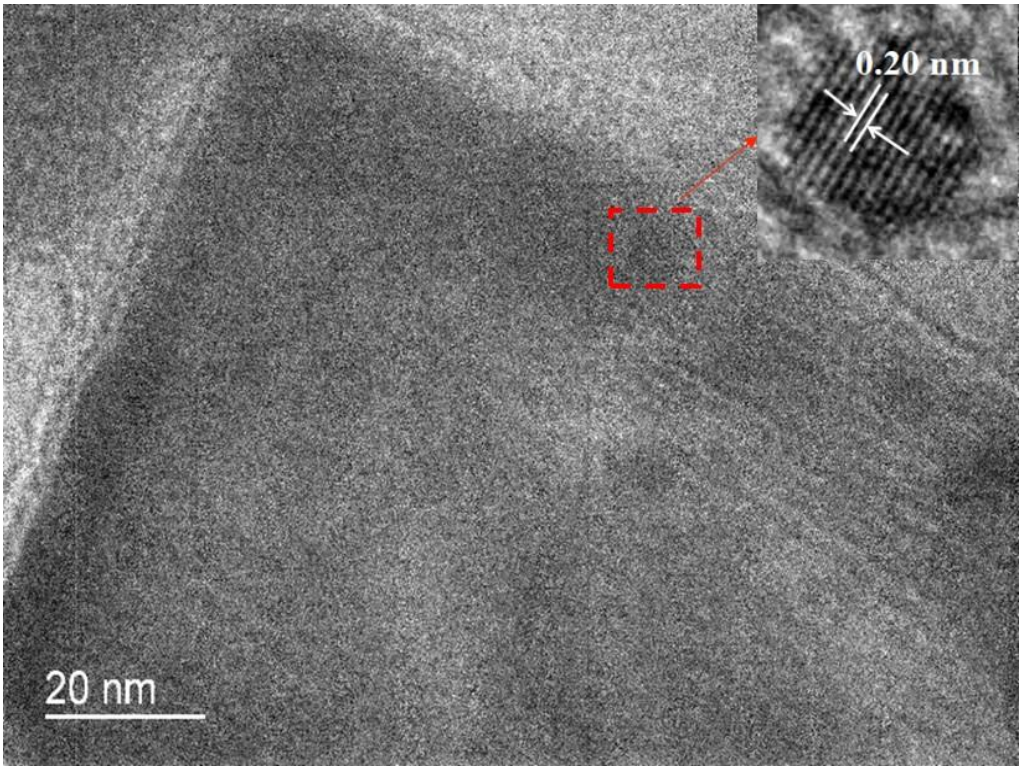

Fig. S2 TEM image of $dWO_3 \bullet H_2O$/N-GQDs nanocomposite. HRTEM image of NGQDs in the nanocomposites.

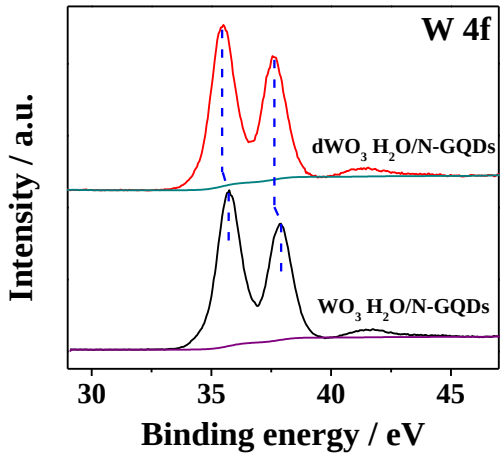

Fig. S3 High-resolution XPS spectra of the W 4f region of $dWO_3 \bullet H_2O$/NGQDs with and without oxygen vacancies.

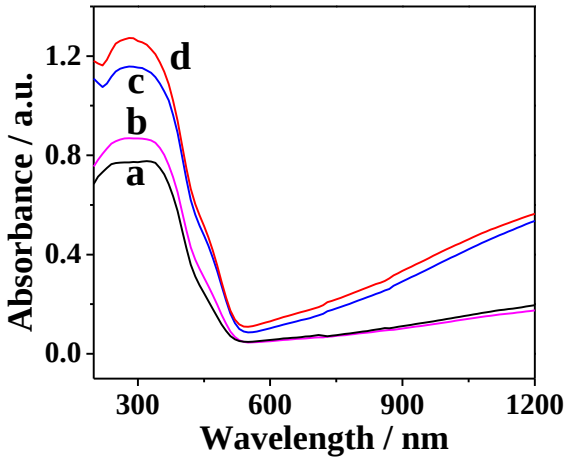

Fig. S4 UV-DRS of the as-prepared $WO_3 \bullet H_2O$ (curve a), $WO_3 \bullet H_2O$/NGQDs (curve b), $dWO_3 \bullet H_2O$ (curve c), and $dWO_3 \bullet H_2O$/NGQDs (curve d).

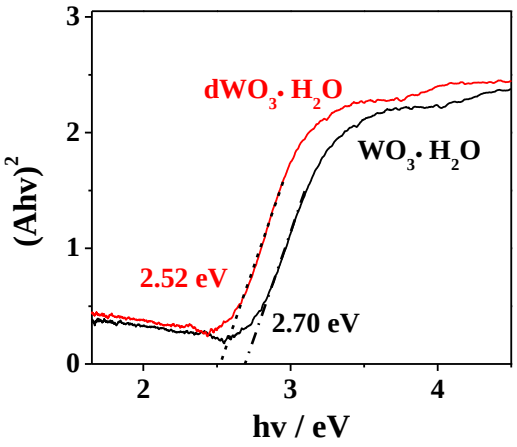

Fig. S5 Optical band gaps determined by UV-vis-IR diffuse reflectance spectra of $WO_3 \bullet H_2O$ and $dWO_3 \bullet H_2O$.

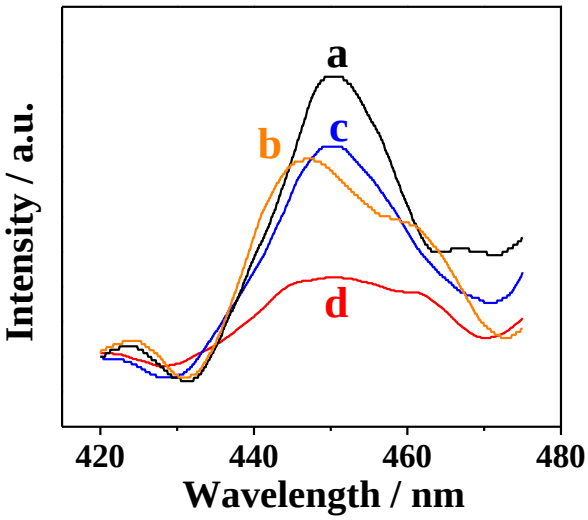

Fig. S6 Photoluminescence spectra of $WO_3 \bullet H_2O$ (curve a), $WO_3 \bullet H_2O$/NGQDs (curve b), $dWO_3 \bullet H_2O$ (curve c), and $dWO_3 \bullet H_2O$/NGQDs (curve d) with an excitation wavelength of 350 nm.